

1 ***Fermi* Large Area Telescope Observations of the Cygnus Loop**
 2 **Supernova Remnant**

3 H. Katagiri^{1,2}, L. Tibaldo^{3,4,5,6,7}, J. Ballet⁵, F. Giordano^{8,9}, I. A. Grenier⁵, T. A. Porter¹⁰,
 4 M. Roth¹¹, O. Tibolla¹², Y. Uchiyama¹⁰, R. Yamazaki¹³

5 Received _____; accepted _____

¹College of Science, Ibaraki University, 2-1-1 Bunkyo, Mito, Ibaraki 310-8512, Japan

²email: katagiri@mx.ibaraki.ac.jp

³Istituto Nazionale di Fisica Nucleare, Sezione di Padova, I-35131 Padova, Italy

⁴Dipartimento di Fisica “G. Galilei”, Università di Padova, I-35131 Padova, Italy

⁵Laboratoire AIM, CEA-IRFU/CNRS/Université Paris Diderot, Service d’Astrophysique,
 CEA Saclay, 91191 Gif sur Yvette, France

⁶Partially supported by the International Doctorate on Astroparticle Physics (IDAPP)
 program

⁷email: luigi.tibaldo@pd.infn.it

⁸Dipartimento di Fisica “M. Merlin” dell’Università e del Politecnico di Bari, I-70126
 Bari, Italy

⁹Istituto Nazionale di Fisica Nucleare, Sezione di Bari, 70126 Bari, Italy

¹⁰W. W. Hansen Experimental Physics Laboratory, Kavli Institute for Particle Astro-
 physics and Cosmology, Department of Physics and SLAC National Accelerator Laboratory,
 Stanford University, Stanford, CA 94305, USA

¹¹Department of Physics, University of Washington, Seattle, WA 98195-1560, USA

¹²Institut für Theoretische Physik and Astrophysik, Universität Würzburg, D-97074
 Würzburg, Germany

¹³Department of Physics and Mathematics, Aoyama Gakuin University, Sagamihara,
 Kanagawa, 252-5258, Japan

To be submitted to ApJ: v6.8, October 31, 2018

6 **ABSTRACT**

7 We present an analysis of the gamma-ray measurements by the Large Area
Telescope (LAT) onboard the *Fermi Gamma-ray Space Telescope* in the region of
the supernova remnant (SNR) Cygnus Loop (G74.0–8.5). We detect significant
gamma-ray emission associated with the SNR in the energy band 0.2–100 GeV.
The gamma-ray spectrum shows a break in the range 2–3 GeV. The gamma-ray
luminosity is $\sim 1 \times 10^{33} \text{erg s}^{-1}$ between 1–100 GeV, much lower than those of
other GeV-emitting SNRs. The morphology is best represented by a ring shape,
with inner/outer radii $0^\circ.7 \pm 0^\circ.1$ and $1^\circ.6 \pm 0^\circ.1$. Given the association among
X-ray rims, $\text{H}\alpha$ filaments and gamma-ray emission, we argue that gamma rays
originate in interactions between particles accelerated in the SNR and interstel-
lar gas or radiation fields adjacent to the shock regions. The decay of neutral
pions produced in nucleon-nucleon interactions between accelerated hadrons and
interstellar gas provides a reasonable explanation for the gamma-ray spectrum.

8 *Subject headings:* cosmic rays — acceleration of particles — ISM: individual objects
9 (the Cygnus Loop) — ISM: supernova remnants — gamma rays: ISM

1. Introduction

Diffusive acceleration by supernova shock waves can accelerate particles to very high energies (e.g., Blandford & Eichler 1987). Gamma-ray observations are a useful probe of these mechanisms complementary to other wavebands. So far, observations by the Large Area Telescope (LAT) on board the *Fermi Gamma-ray Space Telescope* have demonstrated that bright gamma-ray sources coincident with middle-aged supernova remnants (SNRs) interacting with dense molecular clouds (Abdo et al. 2009, 2010a,b,e,f) exhibit steep gamma-ray spectra above a few GeV. A possible conventional explanation for these spectral properties is that the energy distribution of cosmic rays (CR) is greatly influenced by their diffusive transport (e.g., Aharonian & Atoyan 1996; Gabici et al. 2009; Torres et al. 2010; Ohira et al. 2011). On the other hand, these features can also be explained by reacceleration of pre-existing cosmic rays at a cloud shock and subsequent adiabatic compression where strong ion-neutral collisions accompanying Alfvén wave evanescence lead to a steepening of the spectrum of accelerated particles (Uchiyama et al. 2010). Furthermore, using three-dimensional magnetohydrodynamic simulations, Inoue et al. (2010) show that the interaction between a supernova blast wave and inhomogeneous interstellar clouds formed by thermal instability generates multiple reflected shocks, which can further energize cosmic-ray particles originally accelerated at the blast-wave shock and produce the spectral break. Since the gamma-ray bright regions are expected to be different in the aforementioned models, studying SNRs with large apparent sizes can help to disentangle the origin of the spectral features.

The Cygnus Loop (G74.0–8.5) is one of the most famous and well-studied middle-aged SNRs. The size ($\sim 3^\circ$) makes it an ideal candidate for detailed morphological studies in high-energy gamma rays since it is larger than the LAT angular resolution above a few hundred MeV. The large angular offset from the Galactic plane ($b \sim -8^\circ.5$) reduces the

35 problems of background contamination and permits a detailed study of the environment
 36 around the shock region by means of infrared/optical/UV observations. The shell-like X-ray
 37 emission from thermal plasma is prominent in the northern region of the remnant, with a
 38 blowout in the southern rim (Ku et al. 1984). The radio spectrum from the limb-brightened
 39 shells is non-thermal (Keen et al. 1973). No correlation with dense molecular clouds
 40 has been reported, although blast waves on the western limb might encounter molecular
 41 material (Scoville et al. 1977). The distance from the Earth is estimated to be 540_{-80}^{+100} pc
 42 based on the proper motion of optical filaments in conjunction with models of non-radiative
 43 shocks (Blair et al. 2005). The age has been estimated to be $\sim 2 \times 10^4$ yr based on plasma
 44 parameters derived from X-ray data (Miyata et al. 1994) and $\sim 1.4 \times 10^4$ yr based on the
 45 shock model and X-ray measurements (Levenson et al. 1998).

46 Four LAT sources positionally associated with the Cygnus Loop SNR are listed in the
 47 1FGL catalog (Abdo et al. 2010d). In this paper, we report a detailed analysis of *Fermi*
 48 LAT observations in the Cygnus Loop region. First, we briefly describe the observations
 49 and data selection in Section 2. The analysis procedure and the results are presented in
 50 Section 3, with the study of the morphology and spectrum of emission associated with the
 51 Cygnus Loop. Results are then discussed in Section 4 and our conclusions are presented in
 52 Section 5.

53 2. OBSERVATIONS AND DATA SELECTION

54 The LAT is the main instrument on *Fermi*, detecting gamma rays from ~ 20 MeV
 55 to > 300 GeV¹. Details about the LAT instrument and pre-launch expectations for the
 56 performance can be found in Atwood et al. (2009). Compared to earlier high-energy

¹ As noted below in the present analysis we use only events with energies > 200 MeV.

57 gamma-ray telescopes, the LAT has a larger field of view (~ 2.4 sr), a larger effective
58 area (~ 8000 cm² for >1 GeV on-axis) and improved point-spread function (PSF; the 68%
59 containment angle > 1 GeV is smaller than 1°).

60 Routine science operations with the LAT began on August 4, 2008. We have analyzed
61 events in the region of the Cygnus Loop collected from August 4, 2008, to August 1, 2010,
62 with a total exposure of $\sim 6 \times 10^{10}$ cm² s (at 1 GeV). The LAT was operated in sky-survey
63 mode for almost the entire period. In this observing mode the LAT scans the whole
64 sky, obtaining complete sky coverage every 2 orbits (~ 3 hr) and approximately uniform
65 exposure.

66 We used the standard LAT analysis software, the *ScienceTools* version v9r16, publicly
67 available from the *Fermi* Science Support Center (FSSC)², and applied the following event
68 selection criteria: 1) events have the highest probability of being gamma rays, i.e., they
69 are classified in the so-called Pass 6 *Diffuse* class (Atwood et al. 2009), 2) events have a
70 reconstructed zenith angle less than 105° , to minimize the contamination from Earth-limb
71 gamma-ray emission, and 3) only time intervals when the center of the LAT field of
72 view is within 52° of the local zenith are accepted to further reduce the contamination
73 by Earth’s atmospheric emission. We also eliminated two short periods of time during
74 which the LAT detected the bright GeV-emitting GRB 081024B (Abdo et al. 2010c) and
75 GRB 100116A (McEnery et al. 2010) within 15° of the Cygnus Loop. We restricted the
76 analysis to the energy range > 200 MeV to avoid possible large systematics due to the
77 rapidly varying effective area and much broader PSF at lower energies.

²Software and documentation of the *Fermi ScienceTools* are distributed by *Fermi* Science Support Center at <http://fermi.gsfc.nasa.gov/ssc>

3. ANALYSIS AND RESULTS

3.1. Morphological analysis

3.1.1. Method

In order to study the morphology of gamma-ray emission associated with the Cygnus Loop we performed a binned likelihood analysis based on Poisson statistics³(see e.g. Mattox et al. 1996). We used only events above 0.5 GeV (compared to the 0.2 GeV used in the spectral analysis) for the morphological study to take advantage of the narrower PSF at higher energies. For this work we used the instrument response functions (IRFs) P6_V3, which were developed following the launch to address gamma-ray detection inefficiencies that are correlated with background rates (Rando et al. 2009). The analysis was performed over a square region of $12^\circ \times 12^\circ$ width with a pixel size of $0.^\circ 1$. We set the centroid of the region to (R.A., Dec.) = $(21^h 03^m 03^s, 33^\circ 42' 56'')$, 2° shifted from that of the Cygnus Loop toward negative Galactic latitudes to avoid the background given by Galactic diffuse emission and Galactic sources. Figure 1 (a) shows a count map in the 0.5–10 GeV energy band in the region used for the analysis, as well as the position of the Cygnus Loop from radio measurements and point sources in the 1FGL catalog. The four LAT sources, 1FGL J2046.4+3041, 1FGL J2049.1+3142, 1FGL J2055.2+3144 and 1FGL J2057.4+3057, are associated with the Cygnus Loop. Note that no gamma-ray pulsation was found for any of these LAT sources.

³As implemented in the publicly available *Fermi Science Tools*. The documentation concerning the analysis tools and the likelihood fitting procedure is available from <http://fermi.gsfc.nasa.gov/ssc/data/analysis/documentation/Cicerone/>.

3.1.2. Background model

97

98 Although the Cygnus Loop is at intermediate Galactic latitude, the contribution of
 99 the Galactic interstellar emission in the gamma-ray band is still important; it must be
 100 carefully modeled to perform morphological studies. Some of the interstellar gas tracers in
 101 the standard diffuse model provided by the LAT collaboration are not fully adequate for the
 102 Cygnus region, notably the E(B-V) map (Schlegel et al. 1998) because of infrared source
 103 contamination and temperature correction problems in such a massive-star forming region.

104

We therefore constructed a dedicated diffuse emission model. The model is analogous
 105 to the standard LAT diffuse model and it includes: a) an isotropic background, taking
 106 into account the isotropic diffuse gamma-ray emission as well as residual misclassified CR
 107 interactions in the LAT; b) large-scale Galactic inverse Compton emission produced by CR
 108 electrons and positrons upscattering low-energy photons, modeled using the GALPROP
 109 code (e.g. Porter et al. 2008); c) emission from interstellar gas arising from nucleon-nucleon
 110 interactions and electron Bremsstrahlung, which is modeled through spatial templates
 111 accounting for atomic gas and CO-bright molecular gas, partitioned along the line of sight
 112 to separate the Cygnus complex from the segments of the spiral arms in the outer Galaxy
 113 seen in this direction, as well as dark gas traced by visual extinction. With respect to the
 114 standard diffuse model, this one includes higher-resolution H I data (Taylor et al. 2003),
 115 visual extinction as a dark-gas tracer (Rowles & Froebrich 2009; Froebrich & Rowles
 116 2010) and it is specifically tuned to reproduce LAT data in the Cygnus region, including
 117 the region of the Cygnus Loop. All these components, along with individual sources, were
 118 jointly fitted to the LAT data in 10 energy bands over the range 0.1–100 GeV with a free
 119 normalization in each energy bin (except for the inverse Compton model that was kept
 120 fixed). For further details we refer the reader to the dedicated paper (Ackermann et al.
 121 2011), where the model is also discussed in detail in terms of CR and interstellar medium

122 properties. We note that the presence of the Cygnus Loop was taken into account in this
123 study. Several models were considered for the Loop, a combination of point sources and
124 geometric templates such as a disk and a ring, as in the analysis performed in this paper.
125 In this way we verified that the impact of the emission from the Cygnus Loop on the
126 parameters of the global model of the region is small (Tibaldo 2011).

127 The results of this analysis were used to construct two model cubes, as a function
128 of direction and energy, separately accounting for the isotropic and smooth large-scale
129 Galactic inverse-Compton emission (a and b) and the structured emission from the gas (c).
130 Such model cubes are part of the background model used to study the Cygnus Loop in
131 this paper. For each of them we included a free normalization in order to further allow the
132 model to adapt in the different cases we investigated along the paper.

133 In addition to interstellar emission, the background model to study the Cygnus Loop
134 includes individual point-like sources in the 1FGL catalog within 15° of the Cygnus Loop
135 except for the sources associated with the Cygnus Loop itself in the catalog; their positions
136 were kept fixed at those given in the catalog and the spectra of the two gamma-ray pulsars
137 in the region used for the analysis were modeled as power laws with exponential cutoffs
138 leaving all spectral parameters free, while the spectra of the other sources were modeled as
139 power laws leaving the integral fluxes as free parameters and assuming the spectral indices
140 reported in the catalog. Note that, due to the PSF, which is poor compared to other
141 wavelengths and strongly energy dependent, and the presence of a bright and structured
142 background given by the interstellar emission, it is difficult to mask the background
143 sources, and they are instead modeled along with the Cygnus Loop. The resulting model
144 of background emission (i.e. not including emission associated with the Cygnus Loop) is
145 shown in Figure 1 (b). The pulsars J2043+2740 and J2055+25 are the most important
146 point sources in the vicinity, but the amount of events from those sources that fall within

147 the Cygnus Loop (due to the broad low-energy PSF) is only 0.4 % and 0.2 % of the
 148 estimated emission from the Loop, respectively.

149 *3.1.3. Comparison with observations at other wavelengths*

150 Figure 2 shows the count map after subtracting the background emission in a $6^\circ \times 6^\circ$
 151 region centered on the Cygnus Loop, (R.A., Dec.) = $(20^h51^m06^s, 30^\circ41'00'')$, with overlays
 152 of images at different wavelengths: X-rays, $H\alpha$ line, radio continuum at 1420 MHz, infrared
 153 radiation at $100 \mu\text{m}$ and CO 2.6 mm line. The correlation between gamma rays, X-rays
 154 and $H\alpha$ emission is evident. There is correlation among gamma rays and radio continuum
 155 emission in the northern part of the Cygnus Loop. On the other hand, the southern rim
 156 is brighter in radio continuum emission than in gamma rays, a phenomenon that perhaps
 157 might be explained by the existence of another SNR overlapping with the southern part
 158 of the Cygnus Loop (Uyaniker et al. 2002). The CO line intensities were integrated for
 159 velocities with respect to the local standard of rest $-25 \text{ km s}^{-1} < V < 30 \text{ km s}^{-1}$. No
 160 obvious association with CO emission is found; some molecular material is apparently
 161 located on the Western side of the Cygnus Loop, but the relationship is not clear. On the
 162 other hand, some correlation with thermal emission from dust at $100 \mu\text{m}$, which can be
 163 considered as a proxy of total interstellar matter densities, is possible.

164 To quantitatively evaluate the correlation with emission at other wavebands, we fitted
 165 the LAT counts with the different models for the Cygnus Loop on top of the background
 166 model described above. First the Cygnus Loop was modeled with the four 1FGL sources,
 167 and then using the images at other wavelengths as spatial templates assuming a simple
 168 power-law spectrum. Note that we did not use the CO and infrared images as spatial

⁴The velocity corresponding to the distance from the Earth (540 pc) is $\sim 0 \text{ km s}^{-1}$.

169 templates due to clear differences between them and the gamma-ray image as shown in
 170 Figure 2. The resulting maximum likelihood values with respect to the maximum likelihood
 171 for the null hypothesis (no emission associated with the Cygnus Loop) are summarized in
 172 Table 1. The test statistic (TS) values, i.e. $-2\ln(\text{likelihood ratio})$ (e.g. Mattox et al. 1996),
 173 for the X-ray and $H\alpha$ images are significantly larger than for the four 1FGL sources. On
 174 the other hand, the TS for the radio image increases moderately in spite of the association
 175 in the northern rim, confirming that radio continuum structures in the southern rim do not
 176 well correlate with gamma-ray emission.

177 *3.1.4. Geometrical Models*

178 We further characterized the morphology of gamma-ray emission associated with
 179 the Loop by using simple parametrized geometrical models. We started with a uniform
 180 disk/ring assuming a simple power-law spectrum. We varied the radius and location of the
 181 disk and evaluated the maximum likelihood values. In the case of the ring, we varied inner
 182 and outer radii as well. The resulting TS values are reported in Table 1. The TS value for
 183 the ring with respect to the disk shape is $\simeq 12$. Assuming that, in the null hypothesis,
 184 the TS value is distributed as a χ^2 with n degrees of freedom, where n is the difference in
 185 degrees of freedom between the two nested models compared ⁵ ($n = 1$ in the present case),
 186 it would be equivalent to an improvement at $\sim 3.5\sigma$ confidence level. Let us note, however,
 187 that the conversion of TS values into confidence level (or, equivalently, false positive rate)
 188 is subject to numerous caveats, see e.g. Protassov et al. (2002). We will thus take into
 189 account the source morphology uncertainties in the spectral analysis, below. In order to
 190 further illustrate the morphology of the gamma-ray emission, in Figure 3 we show its radial

⁵see link to *Fermi Science Tools* Cicerone

191 profile compared with the best-fit disk/ring models.

192 Finally, we want to verify if there are any spectral variations in the gamma-ray emission
 193 associated with the Cygnus Loop we are modeling as a whole. We thus divided the best-fit
 194 ring into four regions as shown in Figure 4 and allowed an independent normalization and
 195 spectral index for the four portions of the ring. There was no significant improvement of
 196 the likelihood for such a non-uniform ring. The TS value and power-law spectral index for
 197 each of the four regions of the remnant are reported for reference in Table 2. No significant
 198 differences are found between the four spectral indexes. Therefore we adopted the uniform
 199 ring template with maximum likelihood parameters for the whole SNR in the following
 200 spectral analysis.

201 3.2. Spectral analysis

202 To measure the spectrum we made maximum likelihood fits in 8 logarithmically-spaced
 203 energy bands from 0.2 GeV to 100 GeV, using the ring template as the model for the spatial
 204 distribution of the Cygnus Loop. Figure 5 shows the resulting spectral energy distribution
 205 (SED). Upper limits at the 90 % confidence level are calculated assuming a photon index of
 206 2 if the detection is not significant in an energy bin, i.e., the TS value with respect to the
 207 null hypothesis is less than 10 (corresponding to 3.2σ for one additional degree of freedom).
 208 Note that the value of the spectral index has a negligible effect on the upper limits.

209 We identify at least three different sources of systematic uncertainties affecting the
 210 estimate of the fluxes: uncertainties in the LAT event selection efficiency, the morphological
 211 template and the diffuse model adopted for analysis. Uncertainties in the LAT effective
 212 area are estimated to be 10 % at 100 MeV, decreasing to 5 % at 500 MeV, and increasing
 213 to 20 % at 10 GeV and above (Rando et al. 2009). Evaluating the systematic uncertainties

214 due to the modeling of interstellar emission is a challenging task, because interstellar
 215 emission is highly structured and methods used at other wavelengths, like comparisons with
 216 neighboring regions, are not fully adequate in the GeV band. We therefore roughly gauged
 217 the related uncertainties by comparing the results with those obtained by adopting instead
 218 the standard LAT diffuse background models ⁶. We similarly gauged the uncertainties due
 219 to the morphological template by comparing the results with those obtained by using the
 220 best-fit disk template instead of the ring. The total systematic errors are set by adding the
 221 above uncertainties in quadrature. Systematic uncertainties are driven by the imperfect
 222 knowledge of the background emission and, especially below a few hundred MeV, of the
 223 LAT response. In Figure 5 we show the uncertainties obtained following these prescriptions.

224 We probed for a spectral break in the LAT energy band by comparing the likelihood
 225 values of a spectral fit over the whole energy range considered based on a simple power
 226 law and other spectral functions. Note that no systematic uncertainties are accounted for
 227 in the likelihood fitting process. The TS values and best-fit parameters are summarized
 228 in Table 3. The fit with a log-parabola function yields a TS value of ~ 50 compared to a
 229 simple power-law model, which corresponds to an improvement at the $\sim 7 \sigma$ confidence
 230 level. In spite of the uncertainties discussed above in the estimate of the confidence level,
 231 the large TS value is indicative of a significant improvement in the fit. A smoothly broken
 232 power law provides a very slight increase in the likelihood with respect to the log-parabola
 233 function, while a power law with exponential cutoff gives a worse fit. In conclusion, a
 234 simple power law as spectral model can be significantly rejected and from all the different
 235 models with cutoffs we get evidence for a steepening of the spectrum above 2–3 GeV.
 236 We detect gamma-ray emission with a formal significance of 23σ for the above curved

⁶*gll_iem_v02* and *isotropic_iem_v02* available from the FSSC
<http://fermi.gsfc.nasa.gov/ssc/data/access/lat/BackgroundModels.html>

237 spectral shapes. The observed photon flux and energy flux in the 0.2–100 GeV range are
 238 $5.0_{-0.6}^{+0.6} \times 10^{-8} \text{ cm}^{-2} \text{ s}^{-1}$ and $6.5_{-0.6}^{+0.7} \times 10^{-11} \text{ erg cm}^{-2} \text{ s}^{-1}$, respectively.

239 4. DISCUSSION

240 The gamma-ray luminosity inferred from our analysis is $\sim 1 \times 10^{33} \text{ erg s}^{-1}$ between
 241 1–100 GeV, lower by one order of magnitude than observed for other GeV-emitting
 242 SNRs (typically $> 10^{34} \text{ erg s}^{-1}$, Abdo et al. 2009, 2010a,b,e,f). The spatial distribution is
 243 best represented by a ring with inner/outer radii $0^\circ.7 \pm 0^\circ.1$ and $1^\circ.6 \pm 0^\circ.1$, respectively.
 244 This makes the Cygnus Loop the largest gamma-ray emitting SNR observed so far, allowing
 245 us to perform a detailed morphological comparison with emission at other wavelengths.

246 There is a correspondence among gamma-ray emission, X-ray rims and $\text{H}\alpha$ filaments,
 247 indicating that the high-energy particles responsible for gamma-ray emission are in the
 248 vicinity of the shock regions. The Balmer-dominated filaments define the current location
 249 of the blast wave and mark the presence of neutral material. Detailed studies of the
 250 particular locations at the northeast have used these nonradiative shocks as density
 251 probes (Raymond et al. 1983; Long et al. 1992; Hester et al. 1994) and derived post-shock
 252 densities of $\sim 5 \text{ cm}^{-3}$ where gamma-ray emission is expected to be bright due to the
 253 compressed material and high density of accelerated particles.

254 The radio continuum emission, originated by high-energy electrons via synchrotron
 255 radiation, is well correlated with gamma-ray emission in the northern region of the remnant
 256 but not in the southern one. The presence of a second SNR was suggested by Uyaniker et al.
 257 (2002). The two SNRs would be at about the same distance based on the rotation measure
 258 analysis of the radio data (Sun et al. 2006). The lack of correlation between gamma rays
 259 and radio continuum emission in the southern region plausibly implies that the second SNR

260 is not producing significant gamma-ray emission at our current sensitivity. There might be
 261 some correlation between total matter densities as traced by infrared thermal emission from
 262 dust and gamma-ray emission, whereas CO emission does not obviously overlap with the
 263 Cygnus Loop.

264 From these considerations, we argue that the bulk of gamma-ray emission comes from
 265 interactions of high-energy particles accelerated at the shocks of the Cygnus Loop with
 266 interstellar matter or fields in the regions just adjacent to the shocks with a gas density of
 267 $\sim 5 \text{ cm}^{-3}$.

268 To model the broadband emission from the entire SNR we adopt the simplest possible
 269 assumption that gamma rays are emitted by a population of accelerated protons and
 270 electrons distributed in the same region and characterized by constant matter density and
 271 magnetic field strength. We assume the injected electrons to have the same momentum
 272 distribution as protons. This assumption requires a break in the momentum spectrum
 273 because the spectral index in the radio domain, corresponding to lower particle momenta,
 274 is much harder than for gamma rays, which correspond to higher particle momenta.
 275 Therefore, we use the following functional form to model the momentum distribution of
 276 injected particles:

$$Q_{e,p}(p) = a_{e,p} \left(\frac{p}{1 \text{ GeV } c^{-1}} \right)^{-s_L} \left\{ 1 + \left(\frac{p}{p_{\text{br}}} \right)^2 \right\}^{-(s_H - s_L)/2}, \quad (1)$$

277 where p_{br} is the break momentum, s_L is the spectral index below the break and s_H above
 278 the break. Note that here we consider minimum momenta of $100 \text{ MeV } c^{-1}$ since the details
 279 of the proton/electron injection process are poorly known.

280 Electrons suffer energy losses due to ionization, Coulomb scattering, Bremsstrahlung,
 281 synchrotron emission and inverse Compton (IC) scattering. We calculated the evolution of

282 the electron momenta spectrum by the following equation:

$$\frac{\partial N_{e,p}}{\partial t} = \frac{\partial}{\partial p} (b_{e,p} N_{e,p}) + Q_{e,p}, \quad (2)$$

283 where $b_{e,p} = -dp/dt$ is the momentum loss rate, and $Q_{e,p}$ is the particle injection rate.
 284 We assume $Q_{e,p}$ to be constant, i.e., that the shock produces a constant number of
 285 particles until the SNR enters the radiative phase, at which time the source turns off. This
 286 prescription approximates the weakening of the shock and the reduction in the particle
 287 acceleration efficiency, which would be properly treated by using a time-dependent shock
 288 compression ratio (Moraal & Axford 1983). To derive the remnant emission spectrum we
 289 calculated $N_{e,p}(p, T_0)$ numerically, where T_0 is the SNR age of 2×10^4 yr. Note that we
 290 neglected the momentum losses for protons since the timescale of neutral pion production
 291 is $\sim 10^7/\bar{n}_H$ yr where \bar{n}_H is the gas density averaged over the entire SNR shell and is
 292 much longer than the SNR age. Also we do not consider the gamma-ray emission by
 293 secondary positrons and electrons from charged pion decay, because the emission from
 294 secondaries is generally unimportant relative to that from primary electrons unless the gas
 295 density is as high as that in dense molecular clouds and the SNR evolution reaches the
 296 later stages, or the injected electron-to-proton ratio is much lower than locally observed.
 297 The gamma-ray spectrum from π^0 decay produced by the interactions of protons with
 298 ambient hydrogen is calculated based on Dermer (1986) using a scaling factor of 1.84 to
 299 account for helium and heavier nuclei in target material and cosmic rays (Mori 2009).
 300 Contributions from bremsstrahlung and inverse Compton scattering by accelerated electrons
 301 are computed based on Blumenthal & Gould (1970), whereas synchrotron radiation is based
 302 on Crusius & Schlickeiser (1986).

303 First, we consider a π^0 -decay dominated model. The number index of protons in the
 304 high-energy regime is constrained to be $s_H \approx 2.6$ from the gamma-ray spectral slope. The
 305 spectral index of the proton momentum below the break is determined to be $s_L \approx 1.8$ by

306 modeling the radio spectrum as synchrotron radiation by relativistic electrons (under the
 307 assumption that protons and electrons have identical injection spectra). The spectral index
 308 α of the radio continuum emission is ~ 0.4 (Uyaniker et al. 2004), where α is defined as
 309 $S_\nu \propto \nu^{-\alpha}$ with S_ν and ν the flux density and the frequency, respectively. It is difficult to
 310 derive the break momentum of the proton spectrum from the gamma-ray spectrum, since in
 311 the GeV energy band we expect a curvature due to kinematics of π^0 production and decay.
 312 The gamma-ray spectrum provides thus only an upper bound for the momentum break at
 313 $\sim 10 \text{ GeV } c^{-1}$. On the other hand, the momentum break cannot be lower than $\sim 1 \text{ GeV } c^{-1}$
 314 to avoid conflicts with radio data. We adopt a break at the best-fit value, $2 \text{ GeV } c^{-1}$. The
 315 resulting total proton energy, $W_p \sim 2.6 \times 10^{48} \cdot (5 \text{ cm}^{-3}/\bar{n}_H) \cdot (d/540 \text{ pc})^2 \text{ erg}$, is less than
 316 1 % of the typical kinetic energy of a supernova explosion. For an electron-to-proton ratio
 317 $K_{ep} = 0.01$ at $1 \text{ GeV } c^{-1}$, which is the ratio measured at the Earth, the magnetic field
 318 strength is constrained to be $B \sim 60 \text{ } \mu\text{G}$ by radio data. The magnetic field strength of the
 319 undisturbed medium in the northeastern rim was estimated to be $\sim 20 \text{ } \mu\text{G}$ by van der Laan
 320 (1962) based on the measurements of shell thickness and expansion velocities together
 321 with the theory of hydromagnetic shock propagation given the density of the undisturbed
 322 medium $\sim 1 \text{ cm}^{-3}$ (e.g., Hester et al. 1994). The compression behind the shock front
 323 indicates a magnetic field strength similar to the value used above in the modeling. Using
 324 the parameters summarized in Table 4, we obtained the SEDs shown in Figure 6 (a).

325 It is difficult to model the gamma-ray spectrum with a model dominated by electron
 326 bremsstrahlung because the break in the electron spectrum required to reproduce the
 327 gamma-ray spectrum would appear in the radio domain as shown in Figure 6 (b).

328 The gamma-ray spectrum can be reproduced by an inverse Compton dominated
 329 model shown in Figure 6 (c). Gamma-ray emission of IC origin is due to interactions of
 330 high-energy electrons with optical and infrared radiation fields and the cosmic microwave

331 background (CMB). We used in our calculations the first two components as they are
 332 modeled in Porter et al. (2008) at the location of the Cygnus Loop. Since their spectra
 333 are very complex, they are approximated by two infrared and two optical blackbody
 334 components. The flux ratio between the IC and the synchrotron components constrains the
 335 magnetic field to be less than $2 \mu\text{G}$ and requires a low gas density of $\bar{n}_{\text{H}} \sim 2 \times 10^{-2} \text{ cm}^{-3}$
 336 to suppress the electron bremsstrahlung. Although such a low density may exist inside
 337 the remnant based on X-ray observations (e.g., Ku et al. 1984), gamma-ray emission peaks
 338 at the shock regions where the gas density is $\sim 1 - 5 \text{ cm}^{-3}$ (see above). Increasing the
 339 intensity of the interstellar radiation field would loosen the constraint on the gas density.
 340 However, a radiation field about 50 times more intense is required to satisfy the above
 341 assumption on the gas density.

342 To summarize, it is most natural to assume that gamma-ray emission from the Cygnus
 343 Loop is dominated by decay of π^0 produced in nucleon-nucleon interactions of hadronic
 344 cosmic rays with interstellar matter. It should be emphasized that our observations of
 345 the Cygnus Loop combined with the radio data constrain the proton momentum break
 346 to be in the range, $1-10 \text{ GeV } c^{-1}$, despite the lack of association with dense molecular
 347 clouds unlike the other middle-aged SNRs detected with the LAT. Thus in this case
 348 cosmic rays responsible for gamma-ray emission are localized near their acceleration
 349 sites without significant diffusion taking place. The correspondence observed between
 350 gamma rays and $\text{H}\alpha$ emission may be accounted for in the “crushed cloud” scenario by
 351 Uchiyama et al. (2010), although the expected filaments cannot be resolved by current
 352 gamma-ray telescopes. The predictions by Inoue et al. (2010) cannot be directly compared
 353 to the Cygnus Loop since their simulations were performed for environments characterized
 354 by dense clouds. However, the scenario of acceleration by reflected shocks might be
 355 operative, on consideration of X-ray and optical observations (e.g., Graham et al. 1995).

5. CONCLUSIONS

356

357 We analyzed gamma-ray measurements by the LAT in the region of the Cygnus Loop,
 358 detecting significant gamma-ray emission associated with the remnant. The gamma-ray
 359 luminosity is $\sim 1 \times 10^{33} \text{erg s}^{-1}$ between 1–100 GeV, lower than for other GeV-emitting
 360 SNRs studied with LAT data. The morphology of gamma-ray emission is best represented
 361 by a ring with inner/outer radii $0.^{\circ}7 \pm 0.^{\circ}.1$ and $1.^{\circ}6 \pm 0.^{\circ}.1$. The Cygnus Loop is
 362 thus the most extended gamma-ray emitting SNR detected in the GeV band so far and
 363 the morphology of gamma-ray emission can be compared in detail with observations at
 364 other wavelengths. There is correspondence among gamma rays, the X-ray rims and the
 365 $\text{H}\alpha$ filaments, indicating that the high-energy particles responsible for the gamma-ray
 366 emission are in the vicinity of the shock regions.

367

The gamma-ray spectrum has a break in the 2–3 GeV energy range. The decay
 368 of π^0 produced by interactions of hadrons accelerated by the remnant with interstellar
 369 gas naturally explains the gamma-ray spectrum. In this scenario our observations of the
 370 Cygnus Loop indicate that the proton momentum spectrum is steep in the high-energy
 371 regime, with a spectral break which is constrained together with radio continuum emission
 372 in the range 1–10 GeV c^{-1} . The absence of molecular clouds in the areas of gamma-ray
 373 emission (contrary to other middle-aged *Fermi* SNRs) constrains some of the scenarios
 374 invoked to explain the observed spectral properties of GeV emitting SNRs.

375

The *Fermi* LAT Collaboration acknowledges generous ongoing support from a number
 376 of agencies and institutes that have supported both the development and the operation
 377 of the LAT as well as scientific data analysis. These include the National Aeronautics
 378 and Space Administration and the Department of Energy in the United States, the
 379 Commissariat à l’Energie Atomique and the Centre National de la Recherche Scientifique

380 / Institut National de Physique Nucléaire et de Physique des Particules in France, the
381 Agenzia Spaziale Italiana and the Istituto Nazionale di Fisica Nucleare in Italy, the Ministry
382 of Education, Culture, Sports, Science and Technology (MEXT), High Energy Accelerator
383 Research Organization (KEK) and Japan Aerospace Exploration Agency (JAXA) in Japan,
384 and the K. A. Wallenberg Foundation, the Swedish Research Council and the Swedish
385 National Space Board in Sweden.

386 Additional support for science analysis during the operations phase is gratefully
387 acknowledged from the Istituto Nazionale di Astrofisica in Italy and the Centre National
388 d'Études Spatiales in France.

389 We have made use of the *ROSAT* Data Archive of the Max-Planck-Institut für
390 extraterrestrische Physik (MPE) at Garching, Germany. The Digitized Sky Surveys were
391 produced at the Space Telescope Science Institute under U.S. Government grant NAG
392 W-2166. The images of these surveys are based on photographic data obtained using the
393 Oschin Schmidt Telescope on Palomar Mountain and the UK Schmidt Telescope. The
394 plates were processed into the present compressed digital form with the permission of these
395 institutions.

REFERENCES

396

397 Abdo, A. A., et al. (The *Fermi* LAT Collaboration) 2009, ApJ, 706, L1

398 Abdo, A. A., et al. (The *Fermi* LAT Collaboration) 2010, Science, 327, 1103

399 Abdo, A. A., et al. (The *Fermi* LAT Collaboration) 2010, ApJ, 712, 459

400 Abdo, A. A., et al. (The *Fermi* LAT Collaboration) 2010, ApJ, 712, 558

401 Abdo, A. A., et al. (The *Fermi* LAT Collaboration) 2010, ApJS, 188, 405

402 Abdo, A. A., et al. (The *Fermi* LAT Collaboration) 2010, ApJ, 718, 348

403 Abdo, A. A., et al. (The *Fermi* LAT Collaboration) 2010, ApJ, 722, 1303

404 Ackermann, M., et al. (The *Fermi* LAT Collaboration) 2011, submitted

405 Aharonian, F. A., & Atoyan, A. M. 1996, A&A, 309, 917

406 Atwood, W. B., et al. (The *Fermi* LAT Collaboration) 2009, ApJ, 697, 1071

407 Beichman, C. A., Neugebauer, G., Habing, H. J., Clegg, P. E., & Chester, T. J. 1988,
408 Infrared astronomical satellite (IRAS) catalogs and atlases. Volume 1: Explanatory
409 supplement, 1,

410 Blair, W. P., Sankrit, R., & Raymond, J. C. 2005, AJ, 129, 2268

411 Blandford, R. D. & Eichler, D. 1987, Phys. Rep., 154, 1

412 Blumenthal, G. R., & Gould, R. J. 1970, Reviews of Modern Physics, 42, 237

413 Crusius, A., & Schlickeiser, R. 1986, A&A, 164, L16

414 Dame, T. M. 2011, arXiv:1101.1499

- 415 Dame, T. M., Hartmann, D., & Thaddeus, P. 2001, *ApJ*, 547, 792
- 416 de Noyer, L. K. 1975, *ApJ*, 196, 479
- 417 Dermer, C. D. 1986, *A&A*, 157, 223
- 418 Froebrich, D., & Rowles, J. 2010, *MNRAS*, 406, 1350
- 419 Gabici, S., Aharonian, F. A., & Casanova, S. 2009, *MNRAS*, 396, 1629
- 420 Graham, J. R., Levenson, N. A., Hester, J. J., Raymond, J. C., & Petre, R. 1995, *ApJ*, 444,
421 787
- 422 Hester, J. J., Raymond, J. C., & Blair, W. P. 1994, *ApJ*, 420, 721
- 423 Inoue, T., Yamazaki, R., & Inutsuka, S.-i. 2010, *ApJ*, 723, L108
- 424 Keen, N. J., Wilson, W. E., Haslam, C. G. T., Graham, D. A., & Thomasson, P. 1973,
425 *A&A*, 28, 197
- 426 Ku, W. H.-M., Kahn, S. M., Pisarski, R., & Long, K. S. 1984, *ApJ*, 278, 615
- 427 Levenson, N. A., Graham, J. R., Keller, L. D., & Richter, M. J. 1998, *ApJS*, 118, 541
- 428 Long, K. S., Blair, W. P., Vancura, O., Bowers, C. W., Davidsen, A. F., & Raymond, J. C.
429 1992, *ApJ*, 400, 214
- 430 Mattox, J. R., et al. , 1996, *ApJ*, 461, 396
- 431 McEnery, J., Chiang, J., Omodei, N., & Nakamori, T. 2010, *GRB Coordinates Network*,
432 *Circular Service*, 10333, 1 (2010), 333, 1
- 433 Miyata, E., Tsunemi, H., Pisarski, R., & Kissel, S. E. 1994, *PASJ*, 46, L101
- 434 Moraal, H., & Axford, W. I. 1983, *A&A*, 125, 204

- 435 Mori, M., 2009, *Astropart. Phys.*, 31, 341
- 436 Ohira, Y., Murase, K., & Yamazaki, R. 2011, *MNRAS*, 410, 1577
- 437 Porter, T., et al. 2008, *ApJ*, 682, 400
- 438 Protassov, R., van Dyk, D. A., Connors, A., Kashyap, V. L., & Siemiginowska, A. 2002,
439 *ApJ*, 571, 545
- 440 Rando, R. et al., arXiv:0907.0626
- 441 Raymond, J. C., Blair, W. P., Fesen, R. A., & Gull, T. R. 1983, *ApJ*, 275, 636
- 442 Reich, W. 1982, *A&AS*, 48, 219
- 443 Rowles, J., & Froebrich, D. 2009, *MNRAS*, 395, 1640
- 444 Schlegel, D. J., Finkbeiner, D. P., & Davis, M. 1998, *ApJ*, 500, 525
- 445 Scoville, N. Z., Irvine, W. M., Wannier, P. G., & Predmore, C. R. 1977, *ApJ*, 216, 320
- 446 Sun, X. H., Reich, W., Han, J. L., Reich, P., & Wielebinski, R. 2006, *A&A*, 447, 937
- 447 Taylor, A. R., Gibson, S. J., Peracaula, M., et al. 2003, *AJ*, 125, 3145
- 448 Tibaldo, L. 2011, PhD thesis, Universities of Padova and Paris Diderot
- 449 Torres, D. F., Marrero, A. Y. R., & de Cea Del Pozo, E. 2010, *MNRAS*, 408, 1257
- 450 Uchiyama, Y., Blandford, R. D., Funk, S., Tajima, H., & Tanaka, T. 2010, *ApJ*, 723, L122
- 451 Uyaniker, B., Reich, W., Yar, A., Kothes, R., Fürst, E. 2002, *A&A*, 389, L61
- 452 Uyaniker, B., Reich, W., Yar, A., Fürst, E. 2004, *A&A*, 426, 909
- 453 van der Laan, H. 1962, *MNRAS*, 124, 125

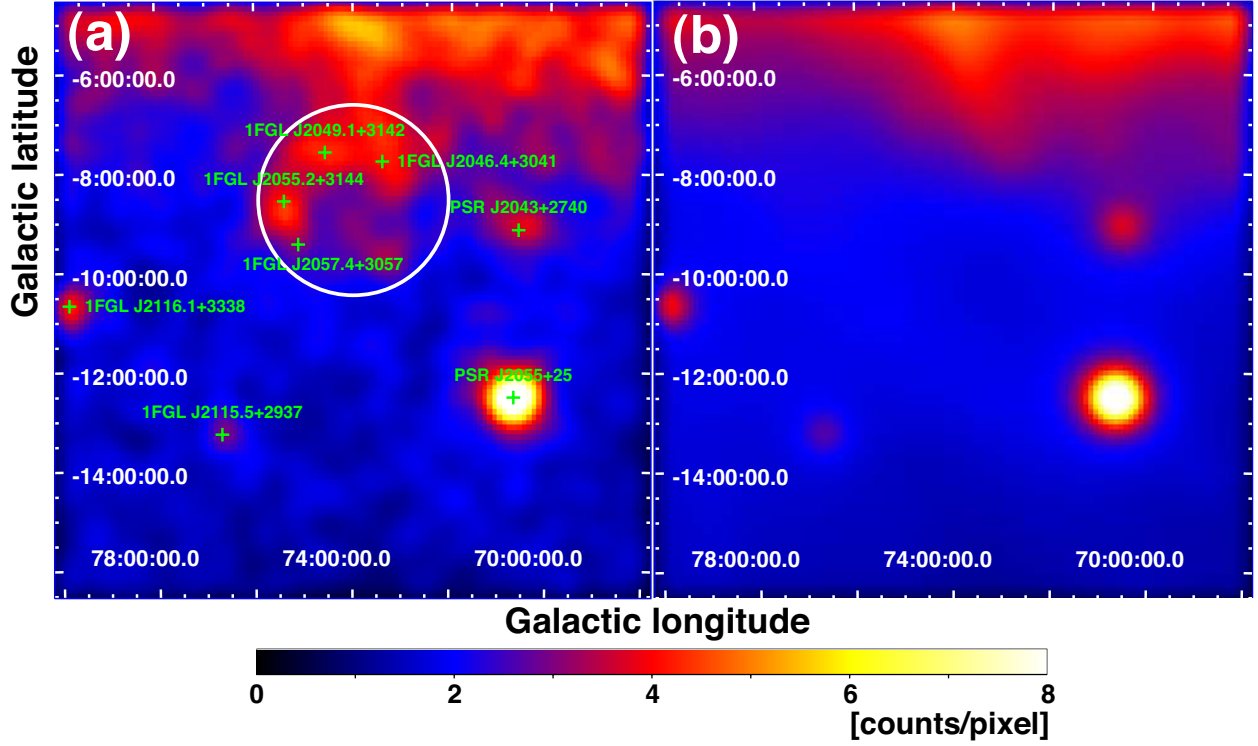


Fig. 1.— (a) *Fermi* LAT count map in the Cygnus Loop region for photon energies 0.5–10 GeV. The count map has a pixel size of $0.^\circ 1$ and is smoothed for display with a Gaussian kernel of $\sigma = 0.^\circ 5$. Note that all along the paper the analysis is conducted on unsmoothed data taking into account the instrument PSF in the likelihood analysis. The white circle is the location of the Cygnus Loop, defined by its radio emission. Green crosses indicate the positions of gamma-ray sources listed in the 1FGL catalog (Abdo et al. 2010d). (b) count map expected from the background model (taking into account the LAT PSF). The four LAT point sources associated with the Cygnus Loop are not included in the model. The image is binned and smoothed in the same manner as the real data.

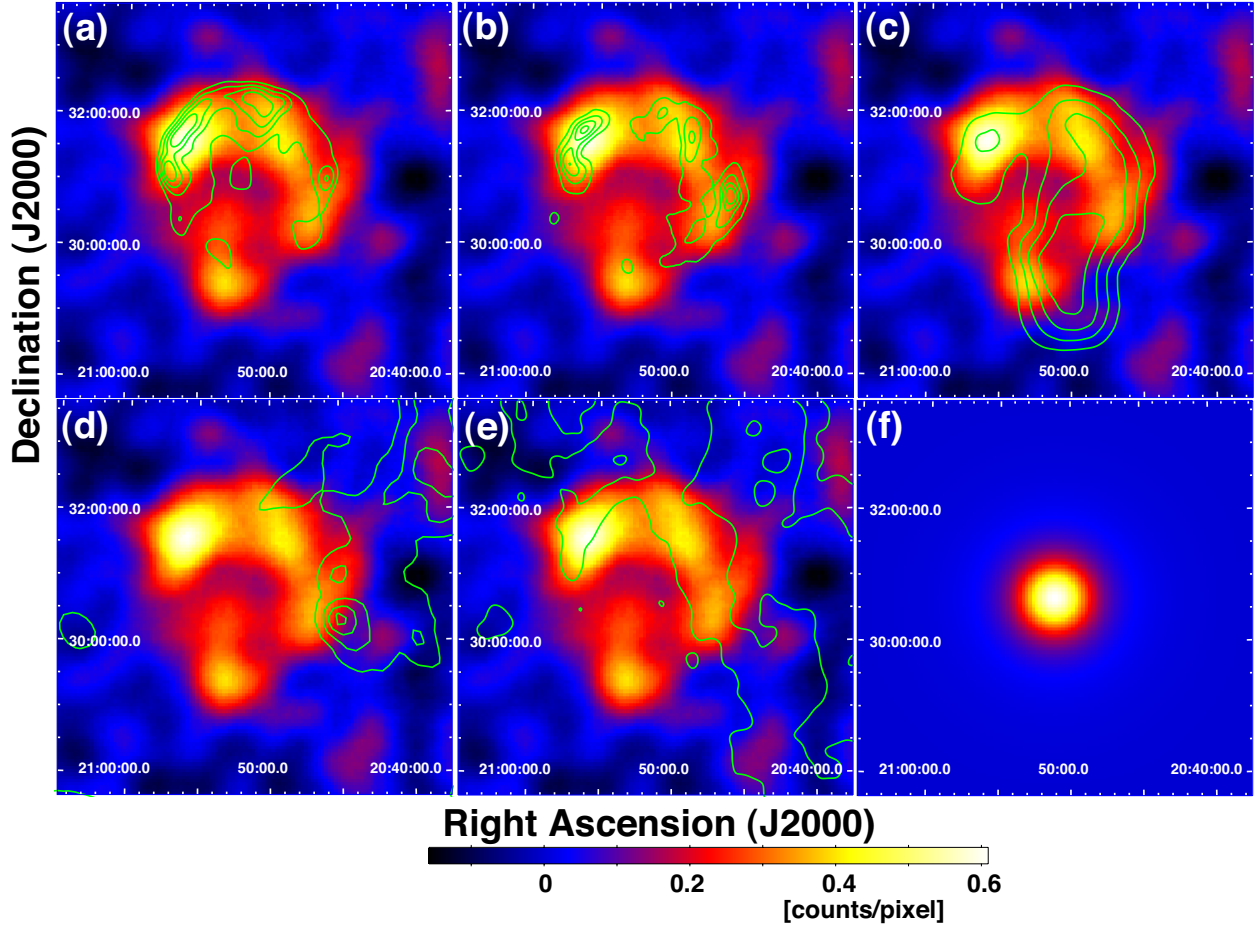


Fig. 2.— Background-subtracted LAT count map in the 0.5–10 GeV energy range. The count map is binned using a grid of $0.^{\circ}05$ and smoothed with a Gaussian kernel of $\sigma = 0.^{\circ}5$. Negative residuals are shown to gauge the quality of the subtraction of the background emission. Green contours correspond to images at different wavelengths. (a) X-ray count map (0.1–2 keV) by *ROSAT*. Contours are at 20, 40, 60, 80 % levels; the image was first cleaned from background emission, estimated by fitting data surrounding the Cygnus Loop with a bilinear function, and smoothed with a Gaussian kernel of $\sigma = 0.^{\circ}2$; (b) $H\alpha$ image obtained from the publicly available Digital Sky Survey obtained with the same procedure explained for X-ray data. We selected the POSS-II F (red) filtered survey whose transmission coefficient peaked near $H\alpha$. (c) 1420 MHz radio continuum emission (Reich 1982); extraction of the contours as for the previous images. (d) ^{12}CO ($J = 1 \rightarrow 0$) line intensities integrated for velocities from -25 km s^{-1} to 30 km s^{-1} . The data are taken from the CfA survey (Dame et al. 2001) cleaned from background using the moment-masking technique (Dame 2011); the image was smoothed using a Gaussian kernel with $\sigma = 0.^{\circ}25$; contours are at 1, 4, 7, 10 K km s^{-1} . (e) The infrared intensity map at $100 \mu\text{m}$ by InfraRed Astronomical Satellite (IRAS) (Beichman et al. 1988); the image was smoothed using a Gaussian kernel of $\sigma = 0.^{\circ}2$; contours are at 15, 25, 35, 45 MJy sr^{-1} . The contour at the top-right corner is the highest one. (f) the effective LAT PSF in the energy band of the LAT count map for a photon spectral index of 2.5. The PSF map is binned and smoothed in the same manner as the real data.

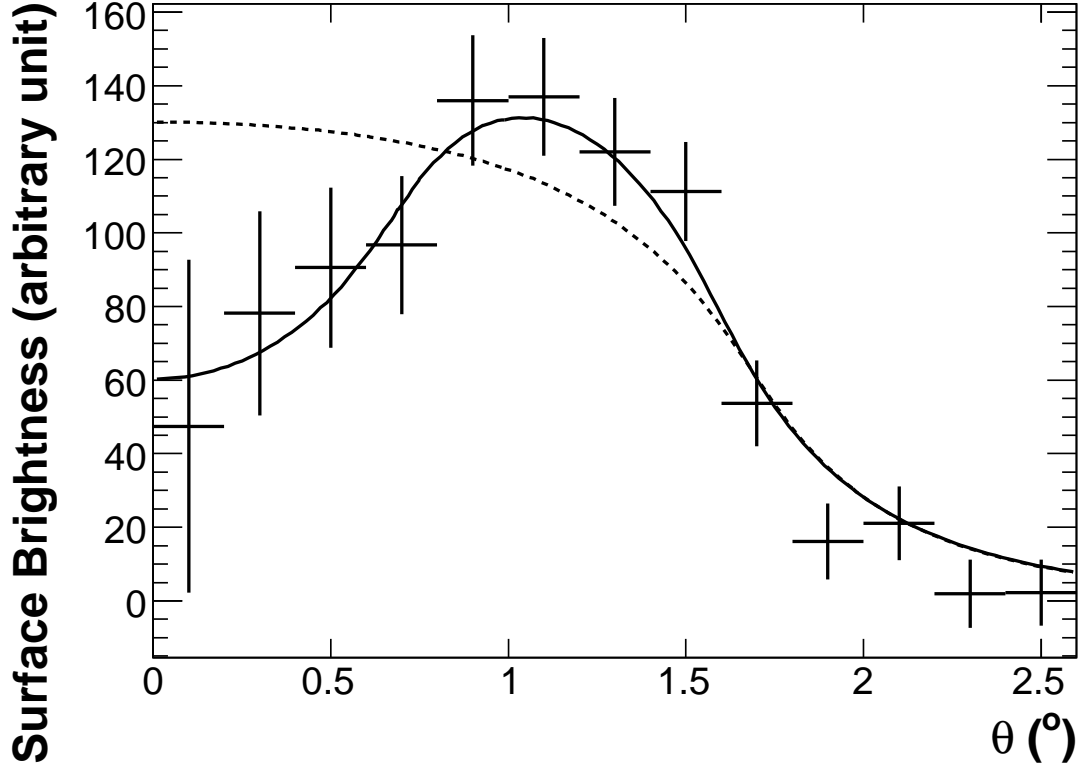


Fig. 3.— Radial profile of the Cygnus Loop in gamma rays in the 0.5–10 GeV energy range (crosses). The origin is the center of the best-fit ring model. Gamma-ray data have the background emission subtracted. Note that the data are not smoothed. Overlaid are the distributions expected for the best-fit ring shape (solid line) and the best-fit disk shape (dotted line) as emission surfaces, with parameters fit to gamma-ray data taking the LAT instrument response into account. Details of the fits are described in the text.

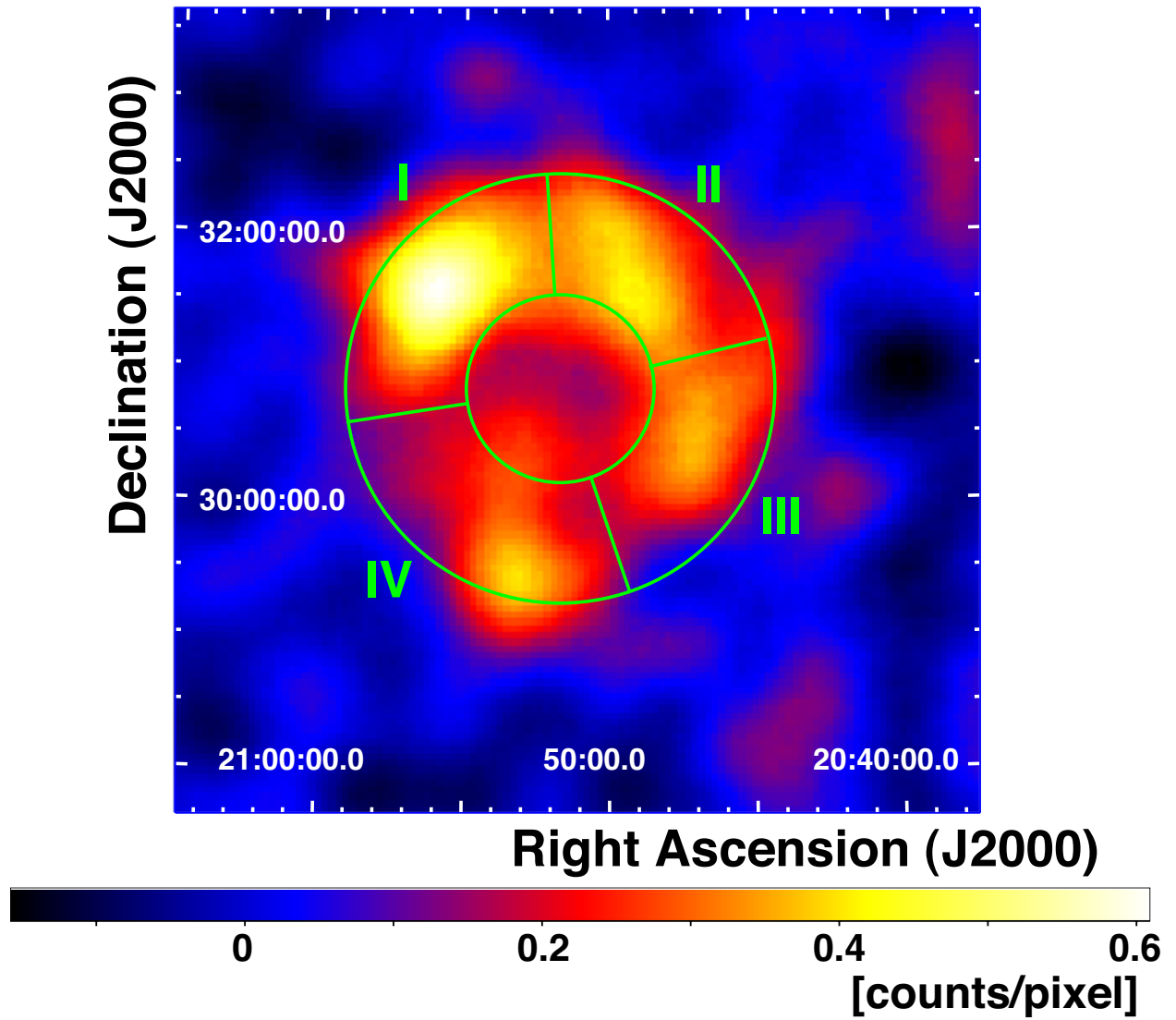


Fig. 4.— Definitions of the regions of the Cygnus Loop used for the morphology analysis (§ 3.1) overlaid on the LAT count map as shown in Figure 2.

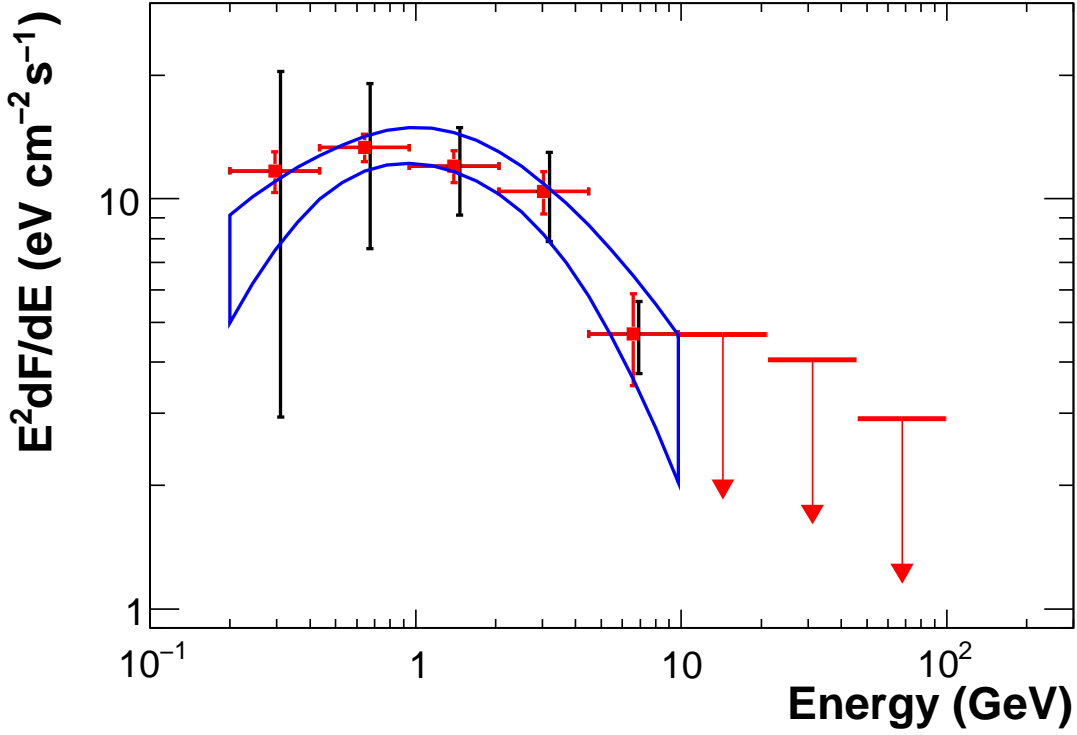


Fig. 5.— Spectral energy distribution of the gamma-ray emission measured by the LAT for the Cygnus Loop. Red squares are LAT flux points. Horizontal bars indicate the energy range the flux refers to. Vertical bars show statistical errors in red and systematic errors (added in quadrature for illustration purposes) in black. In energy bins where the detection is not significant (test statistic < 10) we show upper limits at the 90 % confidence level. The blue region is the 68 % confidence range (no systematic error) of the LAT spectrum assuming that the spectral shape is a log parabola.

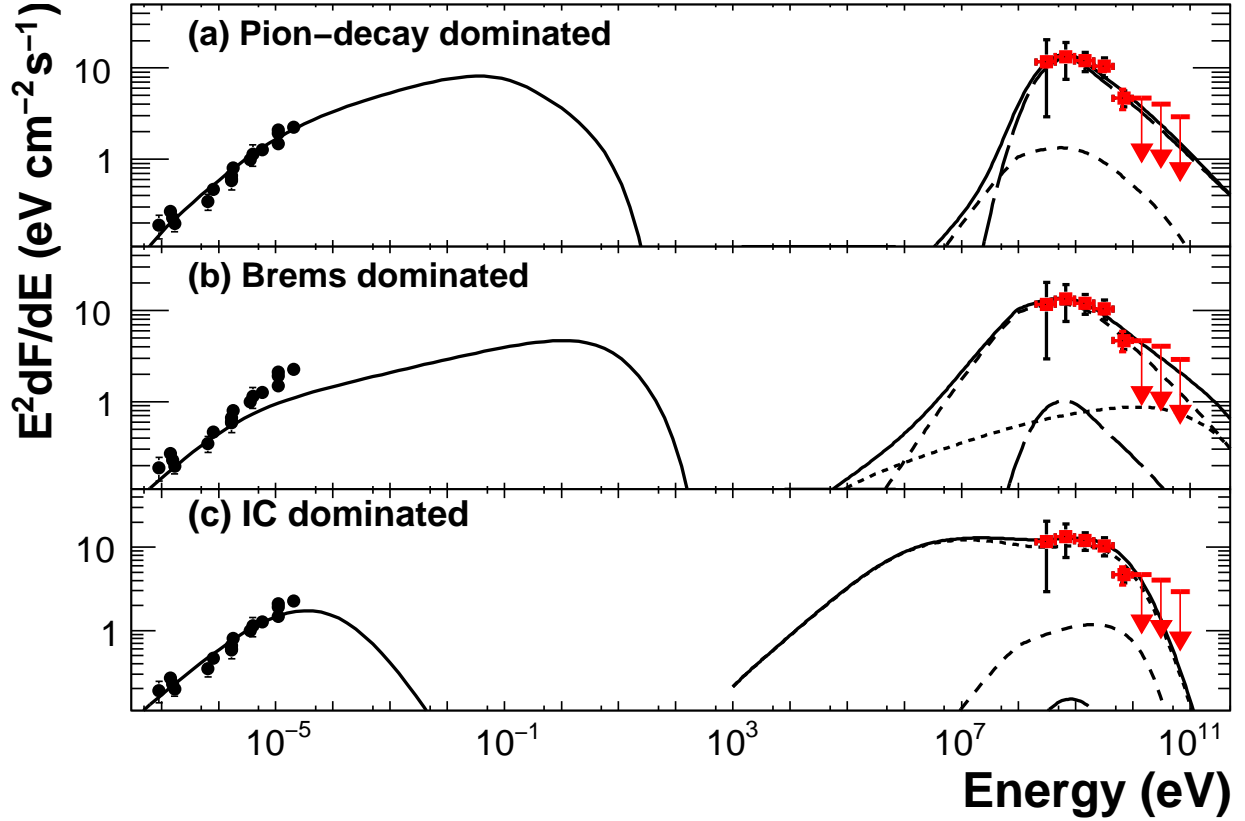


Fig. 6.— Multi-band spectrum of the Cygnus Loop. In the GeV band LAT measurements are reported as in Figure 5. The radio continuum emission (Uyaniker et al. 2004) is shown by black dots. Radio emission is modeled as synchrotron radiation, while gamma-ray emission is modeled by different combinations of π^0 -decay (long-dashed curve), bremsstrahlung (dashed curve), and inverse Compton (IC) scattering (dotted curve). Details of the models are described in the text: a) π^0 -decay dominated model, b) bremsstrahlung dominated model, c) IC dominated model.

Table 1: Test Statistics for Different Spatial Models Compared with the Null Hypothesis of No Gamma-ray Emission Associated with the Cygnus Loop (0.5–100 GeV)

Model	Test Statistic ^a	Additional Degrees of Freedom
Null hypothesis ^b	0	0
4 point sources ^c	318	8
<i>ROSAT</i> X-rays (0.1–2keV) ^d	406	2
H α ^d	434	2
1420MHz radio continuum ^d	343	2
Uniform disk ^e	441	5
Uniform ring ^f	453	6
Non-uniform ring ^g	464	12

^a $-2 \ln(L_0/L)$, where L and L_0 are the maximum likelihoods for the model with/without the source component, respectively.

^bBackground only (no model for the Cygnus Loop).

^cThe four sources listed in the 1FGL source list associated with the Cygnus Loop (Abdo et al. 2010d).

^dBackground-subtracted as described in Figure 2.

^eThe best fit parameters are: radius $1^\circ.7 \pm 0^\circ.1$ and centroid (R.A., Dec.) = $(20^h52^m, 30^\circ50')$. The error of the centroid is $0^\circ.04$ at 68 % confidence level.

^fThe best fit parameters are: inner/outer radii $0^\circ.7 \pm 0^\circ.1$, and $1^\circ.6 \pm 0^\circ.1$, centroid (R.A., Dec.) = $(20^h51^m, 30^\circ50')$. The error of the centroid is $0^\circ.04$ at 68 % confidence level.

^gThe best-fit ring were divided into four regions as shown in Figure 4 and allowed an independent normalization and spectral index for the four portions of the ring.

Table 2: Test Statistics and Power-law Spectral Indexes for the Four Regions of the Remnant as Defined in Figure 4 (0.5–100 GeV)

Region	Test Statistic ^a	Spectral Index
I	143	2.49 ± 0.10
II	73	2.32 ± 0.12
III	64	2.25 ± 0.15
IV	41	2.37 ± 0.14

^a $-2 \ln(L_0/L)$, where L and L_0 are the maximum likelihoods for the model with/without the source component, respectively.

Table 3: Test Statistics and Parameters for Various Spectral Models (0.2–100 GeV)

Spectral Model	Test Statistic ^a	Degrees of Freedom	Spectral Parameters
Power law	0	2	E^{-p} ; $p = 2.23 \pm 0.02$
Power law with exponential cutoff	42	3	$E^{-p} \exp\left(-\frac{E}{E_b}\right)$; $p = 1.57 \pm 0.12$ $E_b = 3.02 \pm 0.65$ GeV
Log Parabola	50	3	$\left(\frac{E}{1 \text{ GeV}}\right)^{-p_1 - p_2 \log\left(\frac{E}{1 \text{ GeV}}\right)}$ $p_1 = 2.02 \pm 0.03$ $p_2 = 0.27 \pm 0.02$
Smoothly broken power law	51	4	$E^{-p_1} \left\{ 1 + \left(\frac{E}{E_b}\right)^{\frac{-p_1 + p_2}{0.2}} \right\}^{-0.2}$ $p_1 = 1.83 \pm 0.06$ $p_2 = 3.23 \pm 0.19$ $E_b = 2.39 \pm 0.26$ GeV

^a $-2\ln(L_0/L)$, where L and L_0 are the maximum likelihood values for the model under consideration and the power-law model, respectively.

Note. — The test statistics for the best-fit uniform ring with exponential cutoff, log parabola, and smoothly broken power law with respect to the null hypothesis of no emission associated with the Cygnus Loop are 572, 580, and 581 in the energy band 0.2–100 GeV.

Table 4: Model parameters for the Cygnus Loop.

Model	K_{ep} ^a	s_L ^b	p_{br} ^c (GeV c^{-1})	s_H ^d	B (μ G)	\bar{n}_H ^e (cm^{-3})	W_p ^f (10^{48} erg)	W_e ^f (10^{48} erg)
(a) Pion	0.01	1.8	2	2.6	60	5	2.6	4.9×10^{-2}
(b) Bremsstrahlung	1	1.8	2	2.7	12	5	0.21	0.43
(c) Inverse Compton ^g	1	1.8	25	5.0	1.8	0.02	5.9	9.8

^aThe ratio electrons-to-protons at 1 GeV c^{-1} .

^bThe momentum distribution of particles is assumed to be a smoothly broken power-law, where the indices and the break momentum are identical for both accelerated protons and electrons. s_L is the spectral index in momentum below the break.

^c p_{br} is the break momentum.

^dSpectral index in momentum above the break.

^eAverage hydrogen number density of ambient medium.

^fThe distance from the Earth is assumed to be 540 pc (Blair et al. 2005). The total energy is calculated for particles > 100 MeV c^{-1} .

^gSeed photons for inverse Compton scattering of electrons include the CMB, two infrared ($T_{IR} = 34, 4.7 \times 10^2$ K, $U_{IR} = 0.34, 6.3 \times 10^{-2}$ eV cm^{-3} , respectively), and two optical components ($T_{opt} = 3.6 \times 10^3, 9.9 \times 10^3$ K, $U_{opt} = 0.45, 0.16$ eV cm^{-3} , respectively) in the vicinity of the Cygnus Loop.